Wideband 3-D-Printed Metal-only Reflectarray for Controlling Orthogonal Linear Polarizations

SUBMISSION DATE / POSTED DATE

30-06-2022 / 07-02-2023

CITATION

Palomares-Caballero, Ángel; Molero Jiménez, Carlos; Padilla, Pablo; García-Vigueras, María; Gillard, Raphaël (2022): Wideband 3-D-Printed Metal-only Reflectarray for Controlling Orthogonal Linear Polarizations. TechRxiv. Preprint. https://doi.org/10.36227/techrxiv.20196173.v2

DOI

10.36227/techrxiv.20196173.v2

This work has been accepted for publication in *IEEE Transactions on Antennas and Propagation*. DOI: 10.1109/TAP.2023.3240583

Wideband 3-D-Printed Metal-only Reflectarray for Controlling Orthogonal Linear Polarizations

Ángel Palomares-Caballero, Carlos Molero, Pablo Padilla, María García-Vigueras, and Raphaël Gillard

***Abstract*—This paper presents a metal-only reflectarray that enables the control of incident orthogonal polarizations in a large bandwidth. The proposed reflectarray is based on a unit cell whose tuning elements allow the independent control of the reflection phase value for the vertical and horizontal impinging polarizations. Due to the symmetry of the unit cell, the same performance is produced by each polarization when its reflection phase response is modified. The proposed unit cell provides a fairly linear phase response along the frequency with a phase variation in the orthogonal polarization of $\pm 1^{o}$. The performance under oblique incidence and the frequency limitation of the unit cell are also investigated. From this unit cell, a metal-only reflectarray that produces circular polarization from a linear polarization is designed. The reflectarray presents a simulated directivity greater than 27 dBi with an axial ratio below 1.5 dB from 32 GHz to 50 GHz (43.9% of bandwidth). A prototype is fabricated and the measured results agree well with the simulated ones. The obtained aperture efficiency is between 56% and 41% in the considered frequency band. The measured realized gain ranges from 27 dBi to 30.3 dBi where the achieved radiation efficiency is greater than 97%.**

***Index Terms*—3D unit cell, dual polarization, metal-only, millimeter-waves, polarization control, reflectarray antenna.**

I. Introduction

REFLECTOR antenna is one of the key radiating element for the future communications paradigms. Both passive [1], [2] and active [3], [4] reflector antennas have been proposed to enhance the link budget in forthcoming wireless communications. Another application in which reflectors or reflectarrays are widely used is in space applications due to the high directivity and versatility provided by this type of antennas [5]. All of the above applications are intended to work in millimeter-wave frequencies to achieve either a higher bandwidth or because the desired frequency is in that range. The direct consequence is the use of metal-only structures in the antennas to obtain greater efficiency [6] and avoid outgassing problems in space applications.

Metal-only reflectarrays have been reported in the literature with different designs and implementations. Following the conventional reflectarray (RA) designs formed by stacked layers of PCBs, [7]–[9] present reflectarrays formed by stacking perforated metallic sheets. Their structures only use metal avoiding dielectric substrates. In [10] and [11], advantage is taken of parallel-plate metallic waveguides to efficiently reflect the incoming wave to broadside and endfire directions, respectively. Metallic square waveguides are also been considered as RA unit cells in [12] and its 3-D printed version in [13], [14] at V-band. An alternative approach to design metal-only RA unit cells is the one proposed in [6] where convex or nonresonant elements are defined. RA designs that employ this geometry for their reflective elements are presented in [15]–[19]. These works demonstrate that large gain bandwidths can be achieved with the adequate choice of the nonresonant element geometry, resulting in a great advantage regarding previous resonant RA unit cells. More complex geometries for metal-only RA unit cells have also been reported. For instance, in [20], a dual-branch helix has been used to obtain a linear phase response along the frequency and preserve the incident circular polarization. Another example is found in [21] where metallic cylinders etched with a rectangular groove provide a stable phase difference and thus, are good candidates to design a two-states RA.

In all the above metal-only reflectarrays, only the phase response of a single polarization can be tuned in the RA design. However, the independent control for orthogonal polarizations of an incident wave in a RA is a desired requirement to extend its functionalities. There are RA unit cells that offer a control of orthogonal polarizations as the one proposed in [22] but, most of them are based on the stacking of PCB layers that have dielectric material in their structure. Nonetheless, in the literature, it is very hard to find this independent polarization control for metal-only RA. The recent development of 3D unit cells offers new possibilities to independently control two orthogonal polarizations and thus, RA unit cells based on this geometry can be developed. The three-dimensional geometry allows a high level for controling orthogonal polarizations as can been observed in dual-band metal-only polarizer in [23]. Based on this design procedure, some metal-only reflectarrays have been conceptually proposed [4] and implemented for a single polarization [24]. However, the design of some of the last RA unit cells are based on resonant elements which provide narrowband performance.

In this paper, a metal-only RA with wideband performance and independent control of incident polarizations is presented. In order to achieve this wideband control of the orthogonal polarizations, the RA unit cells have a 3D geometry which enables the excitation of two orthogonal transverse electro-

This work was supported in part by the Spanish Government under Project PID2020-112545RB-C54 and, Project RTI2018-102002-A-I00, in part by "Junta de Andalucía" under Project B-TIC-402-UGR18, Project A-TIC-608-UGR20, Project PYC20-RE-012-UGR and Project P18.RT.4830, and in part by the Predoctoral Grant FPU18/01965. *(Corresponding author: Ángel Palomares-Caballero.)*

Á. Palomares-Caballero, C. Molero, and P. Padilla are with the Department of Signal Theory, Telematics and Communications, Universidad de Granada, 18071 Granada, Spain (e-mail: angelpc@ugr.es; cmoleroj@ugr.es; pablopadilla@ugr.es).

M. García-Vigueras, and R. Gillard are with UMR CNRS 6164, INSA Rennes, IETR, 35708 Rennes, France (e-mail: Maria.Garcia-Vigueras@insa-rennes.fr; Raphael.Gillard@insa-rennes.fr).

magnetic (TEM) modes. The work in [25] is also based in the excitation of TEM modes in a 3D unit cell in order to achieve broadband polarization conversion. However, such unit cell operated in transmission and its topology was not conceived to operate in reflection. In addition, the purely metallic nature of the proposed RA structure enables an easy and feasible redesign by geometric scaling for tuning in the desired frequency band. To the best of the authors' knowledge, it is the first design of a metal-only RA with wideband performance and independent control of incident orthogonal linear polarizations. The outline of this paper is the following one. Section II presents and discusses the electromagnetic (EM) performance of the proposed RA unit cell. In Section III, the design of a circular-polarized RA is done by means of the proposed RA unit cells. Section IV shows the prototype and its measurements as well as a discussion of the results. Finally, Section IV presents the conclusions from this work.

II. Reflectarray Unit Cell: Design and Analysis

Fig. 1 illustrates the geometric evolution of the proposed RA unit cell from its original design (labelled as (0)) to its optimized design (labelled as (3)). RA unit cell (0) can be seen as a combination of horizontal and vertical parallel plates whose groove depths are varied independently for each polarization. It is similar to the RA unit cells introduced in [10], [11] but here for both x- and y-directions. All the unit cells designs illustrated in Fig. 1 only use metal in their structure. The tuning elements, highlighted in red and green, are metallic blocks whose heights h_{V} and h_{H} are modified to change the phase reflection response of the vertical (V-pol) and horizontal (H-pol) polarizations, respectively. Impinging wave is vertically polarized when the electric field (E-field) is in y-direction while it is horizontally polarized when the E-field is in the x-direction. The propagation of the incident wave is considered in the z-direction and the reflected one is in the minus z-direction. In the performed EM simulations, periodic environment is applied along the x- and y-directions since the local periodicity approach is widely used in the literature for analysing quasi-periodic structures such as reflectarrays. The EM software used in all the simulations of the paper is CST Studio Suite whose Frequency Solver is employed for the RA unit cell simulations while the Time Solver, for the complete RA design. The design procedure for both RA unit cell and complete RA is aimed for the frequency band from 32 GHz to 50 GHz. This frequency range corresponds to the full operating frequency band of the WR22 waveguide standard.

Coming back to the RA unit cell evolution shown in Fig.1, geometric modifications have been introduced from (0) to (3) unit cell designs. These modifications have an impact in the EM performance of the original RA unit cell. Fig. 2 shows the reflection phase response of each RA unit cell design when the parameter h_{V} varies, keeping the value of parameter h_{H} fixed in the sweep. Due to the desired independent phase response of each polarization, the phase response for the H-pol should not be changed. In order to clearly observe this fact, the phase difference for the H-pol is also included in Fig. 2 in which the phase response reference is the case when h_{H} is

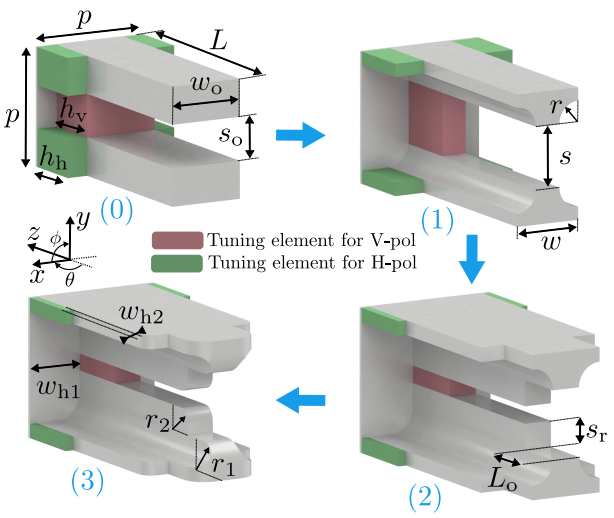

Fig. 1. Design evolution of the proposed RA unit cell. The dimensions are: $p = 4$, $w_{\mathrm{o}} = 2.54$, $L = 7.6$, $s_{\mathrm{o}} = 1.46$, $w = 2.1$, $s = 1.92$, $r = 0.64$, $s_{\mathrm{r}} = 0.72$, $L_{\mathrm{o}} = 1.52$, $r_1 = 0.64$, $r_2 = 0.4$, $w_{\mathrm{h1}} = 1.6$ and, $w_{\mathrm{h2}} = 0.24$. All dimensions are in mm.

minimum. Notice that all the RA unit cell designs presented in Fig. 1 are symmetric both for x- and y-directions and thus, it is enough to analyze the variation of one of the tuning parameters, h_{V} in our case. Figs. 2(a) and 2(b) show the EM performance for both orthogonal polarizations. It can be observed that the phase range is approximately 720º because the length of the RA unit cell L is almost one wavelength at the center frequency. Nevertheless, the phase response along the frequency illustrated in Fig. 2(a) is quite nonlinear with an inadequate phase difference to achieve the independent control of both polarizations (see Fig. 2(b)). For RA unit cell (1), the reflection phase response and the phase variation of the orthogonal polarization are displayed in Figs. 2(c) and 2(d), respectively. With the inclusion of roundness with a radius r on the edges of the parallel plate, a higher linearity in the phase response can be achieved and also, a decrease in the variation of the phase response for the H-pol. The separation between parallel plates for this RA unit cell is also greater ($s > s_{\mathrm{o}}$) providing a better impedance matching with free space and thus, enhancing the phase linearity along the frequency [26]. Figs. 2(e) and 2(f) display the phase behaviour of both polarizations for the RA unit cell (2). The only geometrical modifications regarding the RA unit cell (1) is the narrowing of the separation between parallel plates (labelled as s_{r} in Fig. 1) starting from a particular distance L_{o} from the beginning of the unit cell design. This inclusion produces an improvement of the phase linearity along the frequency as can be observed in Fig. 2(e) and a reduction of the phase difference in the phase response of the H-pol shown in Fig. 2(f). This enhancement in the phase response is at expense of limiting the length range of the tuning parameter h_{V}. However, it is not a problem because the tuning phase response is still beyond 360º, required value for a suitable RA design. An additional design improvement can be done by rounding the edges of the ends of the parallel-plate waveguides by r_1 and r_2 as it is illustrated in the RA unit cell (3) of Fig. 1. In this way, the linear phase response

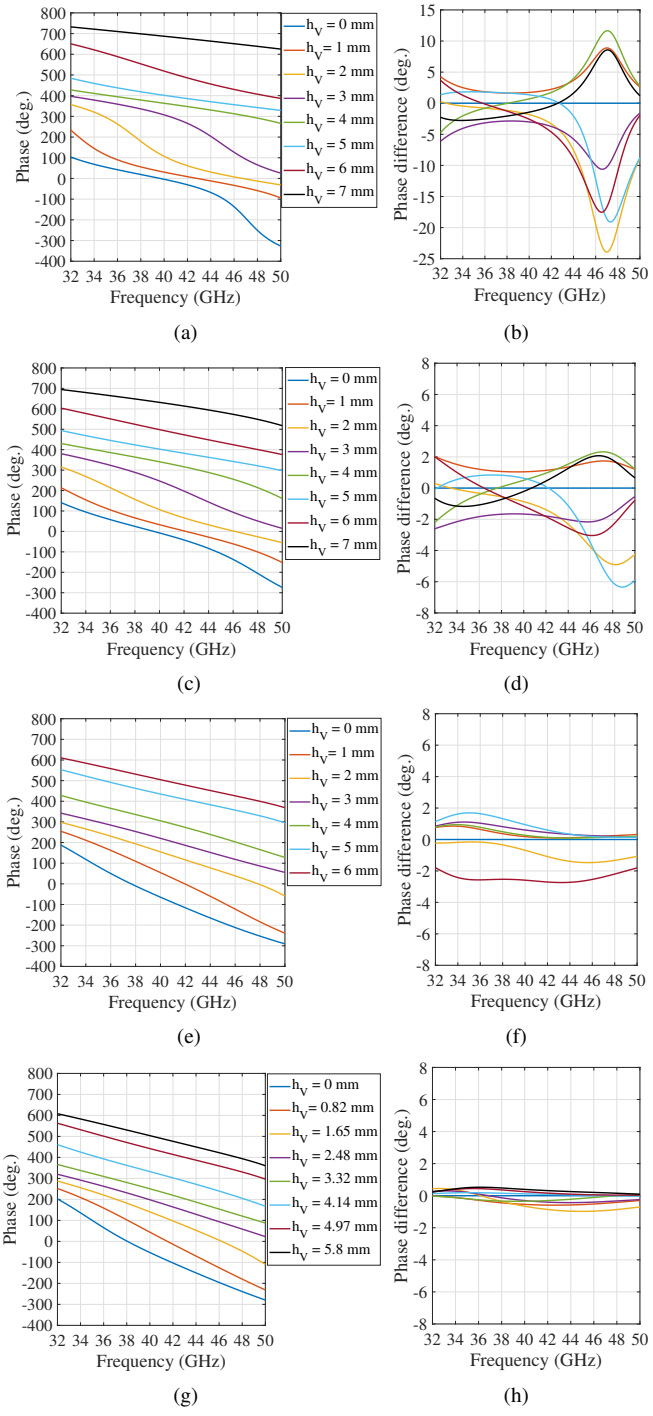

Fig. 2. Reflection phase response with a V-pol plane wave excitation under a normal incidence when tuning length h_V is modified: (a) RA unit cell (0), (c) RA unit cell (1), (e) RA unit cell (2) and, (g) RA unit cell (3). Phase difference in the orthogonal polarization (H-pol) when tuning length h_V is modified: (b) RA unit cell (0), (d) RA unit cell (1), (f) RA unit cell (2) and, (h) RA unit cell (3).

is preserved as it is shown in Fig. 2(g) and the phase response difference in the H-pol is further enhanced by reducing the range of variation between +0.5° and -1°. Therefore, this RA unit cell design meets the desired requirements and it is the one selected for the RA antenna design.

The magnitude performance of the selected RA unit cell is

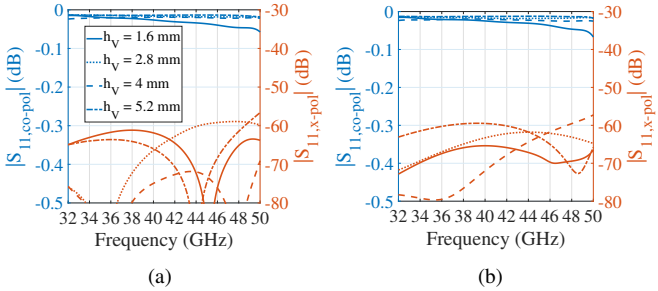

Fig. 3. Co-polarized and cross-polarized reflection in magnitude of the RA unit cell (3) in: (a) normal incidence and, (b) oblique incidence ($\phi = 90^o$ and $\theta = 20^o$).

shown in Fig. 3. It can be seen that the cross-polar component has a negligible excitation since it is below -60 dB over the considered bandwidth. The performance is similar to the unit cell presented in [27] because of the employed 3D geometry. This fact is preserved for different values of h_V and for oblique incidence situations as displayed in Fig. 3(b).

Fig. 4 shows the E-field distribution of the selected RA unit cell when it is illuminated by a V-pol plane wave. The E-field distributions have been plotted at different planes of interest (H, V_0 and V_1) indicated in Fig. 4(a). The vector and the magnitude distributions of the y component of the E-field are illustrated in Fig. 4(b). From this figure, it can be realized that the electric field is propagating mainly along the parallel-plate waveguide (subfigure framed in orange and blue). In contrast, in the V_1 plane, which contains the propagating path for the H-pol, the V-pol can hardly propagate with the magnitude of the E-field being close to zero as shown in the subfigures framed in green included in Fig. 4(b). This fact is due to the mode field distribution when the V-pol plane wave is impinged on the RA unit cell. Almost all the power propagates along the conductors that form the parallel plate waveguide where the tuning element is placed. On both sides of this waveguide, the E-field decays strongly in the x-direction as can be seen in the plane H of Fig. 4(b). Beyond the tuning element, the E-field distribution between RA unit cells is rapidly attenuated because the mode becomes evanescent since it becomes a TE_{10} waveguide mode whose waveguide width is $2w_{h1}$. This can be observed in the waveguide zone indicated in the planes V1 and H of Fig. 4(b). The same rationale is valid for an illumination of the RA unit cell with a H-pol plane wave. All above observations give an explanation about the remarkable isolation in the phase response tuning of the incident orthogonal polarizations.

The electric field distribution analyzed in the unit cell shows that the highest electric field intensity is located in the gap of the parallel-plate waveguide. The size of this gap determines the maximum power-handling capacity before multipactor phenomenon appears, which is of particular concern in satellite applications. Using the commercial software SPARK3D, the calculation of the multipactor power threshold is performed. At 41 GHz, the maximum power-handling capacity is 8699 W.

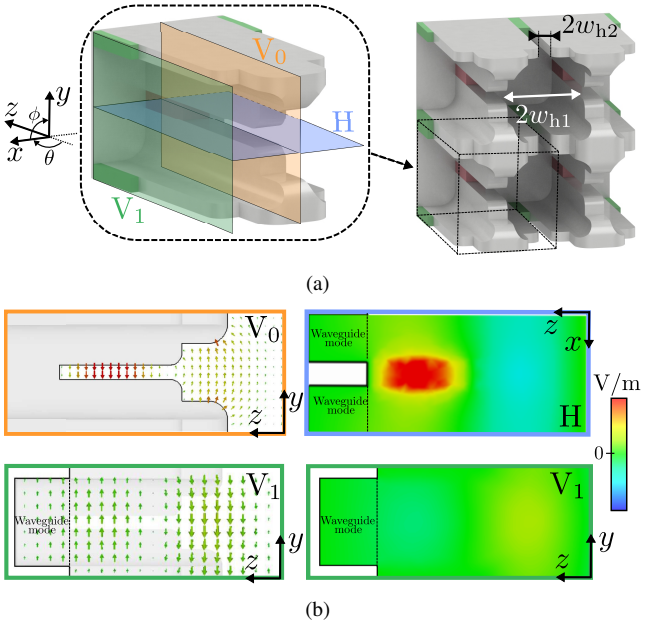

Fig. 4. (a) 3-D view of the proposed reflectarray unit cells and some of the planes of interest. (b) E-field distribution in the planes of interest when a V-pol plane wave impinges the unit cell under normal incidence. The subfigures on the left are vector plots while the subfigures on the right are magnitude plots

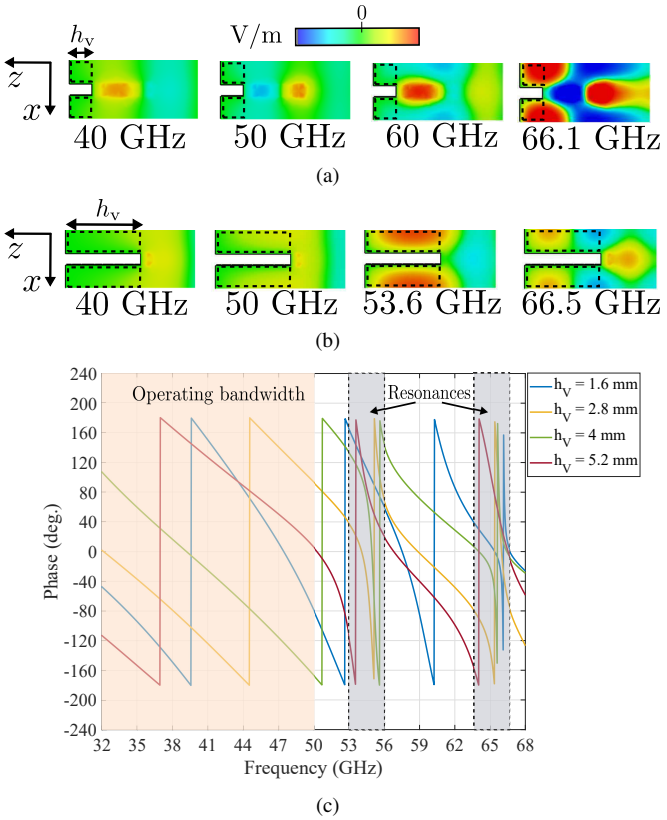

Fig. 5. E-field distribution of unit-cell environment of two cells in the plane of interest H at different frequencies: (a) when $h_V = 1.6$ mm and, (b) when $h_V = 5.2$ mm. (c) Phase response of the proposed RA unit cell in an extended frequency range. The excitation of the unit cell is a V-pol plane wave under normal incidence.

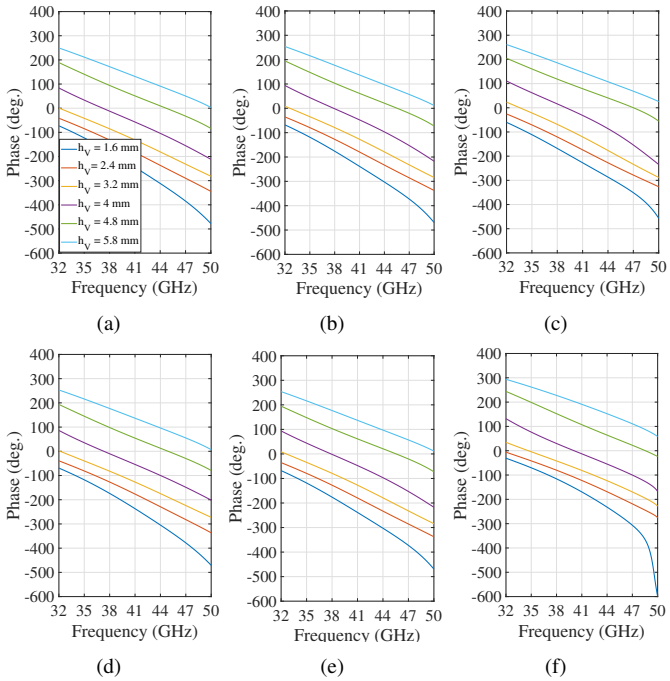

Fig. 6. Reflection phase response of the proposed reflectarray unit cell under oblique incidence when h_V varies. Oblique incidence in the E-plane ($\phi = 90^o$) where: (a) $\theta = 10^o$, (b) $\theta = 20^o$ and, (c) $\theta = 30^o$. Oblique incidence in the H-plane ($\phi = 0^o$) where: (d) $\theta = 10^o$, (f) $\theta = 20^o$ and, (g) $\theta = 30^o$. The excitation is a V-pol plane wave.

A. Resonances in the unit cell

As described above, the selected RA unit cell mostly allows the wave propagation along its structure to the polarization whose E-field is perpendicular to the parallel-plate waveguide (see Fig. 4(b), subfigure framed in orange). Nevertheless, although in the regions where the E-field amplitude is very weak or even evanescent, some cavity resonances can be generated if the resonance conditions are fulfilled for a certain frequency. In Figs. 5(a) and 5(b), the plane of interest H is displayed for a unit-cell environment of two cells with different length for the tuning element and at different frequencies. It can be seen how the large part of the incident E-field tends to propagate along the area of the parallel plate waveguides. However, when the frequency increases or the tuning length h_V is longer, some resonances appear in the evanescent regions, i.e., the regions enclosed with dashed line in Figs. 5(a) and 5(b). These resonances completely alter the linear phase response of the unit cell as displayed in Fig. 5(c). The reflection coefficient in phase for different tuning length values has been investigated and all the possible resonances between unit cells occur outside of the operating bandwidth. This physical insight reveals the performance limitation in frequency of the proposed RA unit cell. Nonetheless, the operating frequency band where the reflection phase produces an acceptable phase linearity is from 32 GHz to 50 GHz, this is, a 43.9% bandwidth.

B. Oblique incidence performance

Fig. 6 presents the reflection phase behavior of the selected RA unit cell under oblique incidence. Figs. 6(a), 6(b) and

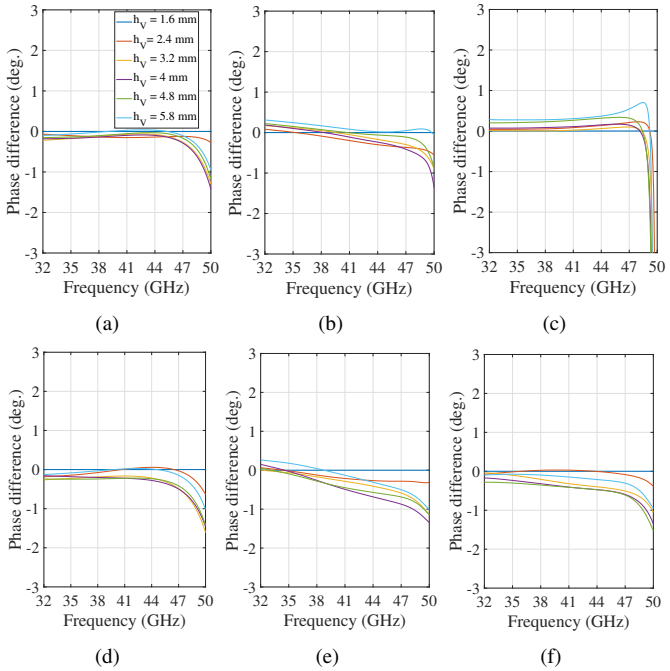

Fig. 7. Phase difference in the orthogonal polarization of the proposed reflectarray unit cell under oblique incidence when h_V varies. Oblique incidence in the E-plane ($\phi = 90^o$) where: (a) $\theta = 10^o$, (b) $\theta = 20^o$ and, (c) $\theta = 30^o$. Oblique incidence in the H-plane ($\phi = 0^o$) where: (d) $\theta = 10^o$, (f) $\theta = 20^o$ and, (g) $\theta = 30^o$. The excitation is a V-pol plane wave.

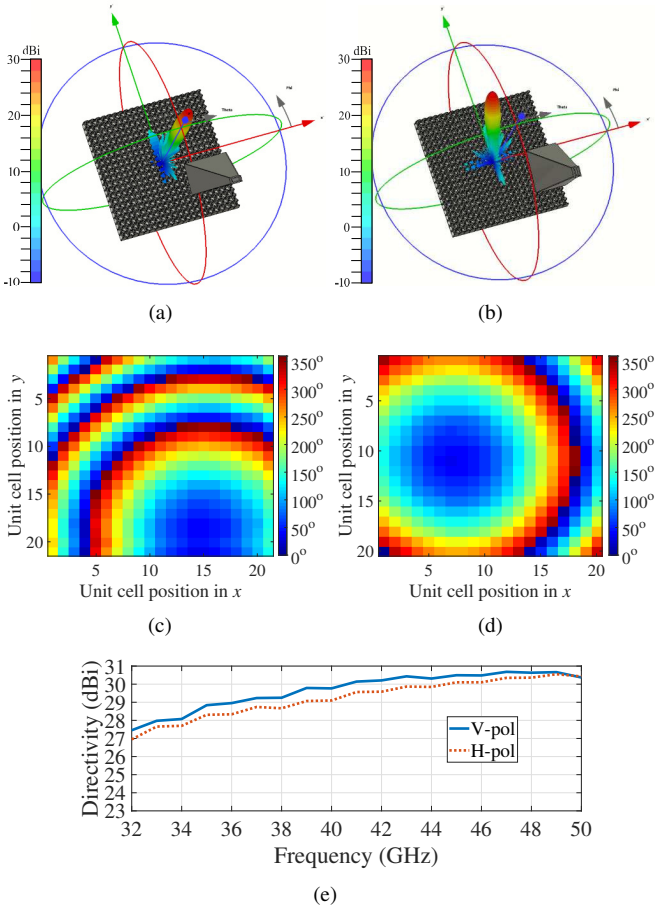

Fig. 8. Simulated 3-D radiation pattern at 41 GHz of a reflectarray based on the proposed RA unit cell: directivity (a) for V-pol and, (b) for H-pol. Their reflected beam directions are ($\phi = 45^o$, $\theta = 10^o$) and ($\phi = 105^o$, $\theta = 20^o$), respectively. The phase maps required for (c) V-pol and, (d) for H-pol. (e) Simulated directivity along the frequency for both incident linear polarizations.

6(c) correspond to oblique incidence in the E-plane while, Figs. 6(d), 6(e) and 6(f) correspond to oblique incidence in the H-plane. E-plane stands for the YZ plane ($\phi = 90^o$ and θ varies) and H-plane stands for the XZ plane ($\phi = 0^o$ and θ varies) of the axis illustrated in Fig. 1. Observing the simulated results for both planes and different oblique incidence angles, the linear phase response is maintained along the frequency range for the different tuning lengths and approximately preserving the phase difference between curves. As expected, as the value of the angle of incidence increases, the performance deteriorates especially for the high end of the frequency range where the slope of the phase curves starts to increase. This is a consequence of the frequency approach of the out-of-band resonances towards the operating bandwidth. For the sake of completeness, the phase difference for the orthogonal polarization is presented in Fig. 7 under the same oblique incidence conditions shown in Fig. 6. Notice that the independent control of the orthogonal polarization is kept and the absolute phase difference is not more than 2º for almost all the oblique incidence cases under study. The only case that exceeds this error at the end of the frequency range is the one presented in the Fig. 7(c). A huge increase in the phase difference appears near 50 GHz. This fact is also a consequence, in this particular case of oblique incidence, of a displacement of the out-of-band resonances closer to the operating bandwidth. The behavior presented above is for a V-pol plane wave impinging on the RA unit cell. The same performance is obtained in the case of an H-pol plane wave excitation due to the symmetry exhibited by the RA unit cell design.

C. Independent beam control by incident polarization

Thanks to the wideband linear phase-response of the selected unit cell and its independent control of orthogonal polarizations, an example of RA design where the reflected beam for each linear polarization has different outgoing direction is shown in Fig. 8. A more detailed view of the RA system can be seen in Fig. 9(a) except that the directions for the V-pol and H-pol linear polarizations are ($\phi = 45^o$, $\theta = 10^o$) and ($\phi = 105^o$, $\theta = 20^o$), respectively. The phase maps required in each polarization to achieve the above-mentioned directions are shown in Figs. 8(c) and 8(d). Lastly, Fig. 8(e) presents the directivity achieved by the RA over the considered frequency range. We observe a similar directivity for both polarizations with the same behavior along the frequency.

III. Circularly-Polarized Reflectarray Design

Complementary to the previous subsection II.C, this section is devoted to the design and analysis of a RA that provides a circular polarization from a linear polarization. In order to generate the circularly-polarized reflected wave, the RA is rotated by 45º regarding the feed antenna which has a linear polarization. In this manner, both orthogonal polarizations are

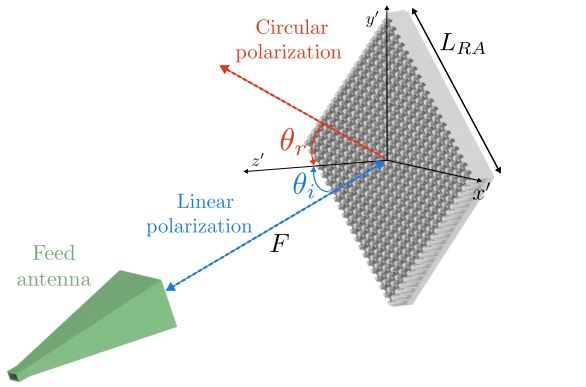

(a)

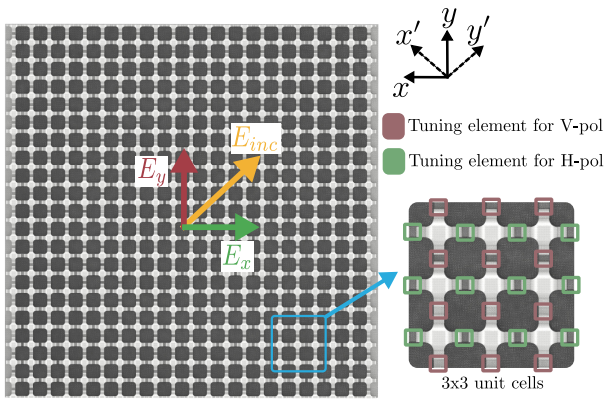

(b)

Fig. 9. (a) 3D view of the reflectarray system. (b) Front view of the proposed reflectarray design. The dimensions are: F = 123.2 mm, L_{RA} = 84 mm, and $\theta_i = \theta_r = 20^{\text{o}}$.

excited in the RA structure [22]. Additionally, to improve the blockage efficiency, the feed antenna illuminates the RA with an offset angle $\theta_i = 20^{\text{o}}$. Fig. 9(a) illustrates the depicted RA system whose selected feed antenna is a commercial 20 dBi horn antenna (Flann WR22 Standard Gain Horn). The distance between the RA and the center of the horn antenna aperture is F [see caption of Fig. 9] and F/L_{RA} =1.47, which ensures an amplitude taper from the center of the RA to the edges approximately equal to -10 dB at the center frequency. The reflected angle of the beam θ_r radiated by the RA has been chosen to be equal to the incident angle ($\theta_r = \theta_i$) and in the same radiation plane, that is, the Z'Y' plane in Fig. 9(a). If a direction other than the specular direction is chosen for the reflected beam, a beam squint with frequency will appear [28], which will be more noticeable the more different is the direction selected regarding to the specular one. The total number of RA unit cells employed in the RA design has been set to 21x21 and thus, at 32 GHz and 50 GHz, the electric size of the RA is 9λ x 9λ and 14λ x 14λ, respectively.

In order to achieve an increase in the directivity of the feed antenna and transform the linear polarization received in the RA to a circular polarization, the phase maps for the V-pol and H-pol have to be carefully calculated. Firstly, the phase map calculation of a single polarization, for instance V-pol, has been considered. The phase of the incident wave

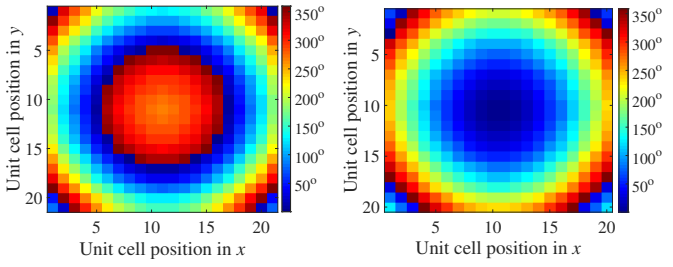

(a) (b)

Fig. 10. Phase maps in reflectarray at 41 GHz: (a) for V-pol and, (b) for H-pol.

at the center of each V-pol tuning element is obtained by simulation. In Fig. 9(b), these tuning elements are highlighted for a RA zone of 3x3 unit cells. In the same figure, the decomposition of the incident E-field (E_{inc}) into the E-field for the V-pol (E_y) and H-pol (E_x) is also displayed. The simulated phases are obtained at 41 GHz, the center frequency of the operating bandwidth. In this manner, a more accurate design in terms of phase correction in the RA is possible when compared to the phases calculated through ray tracing method [29]. Once the incident phases are obtained, the phase map of the RA is computed since the positions of RA unit cells and the direction of the reflected beam is known [5]. For the orthogonal polarization (H-pol), a similar procedure is done. The phases obtained from the simulation are the ones corresponding to the central zones of the tuning elements for H-pol. To produce the circular polarization, both orthogonal polarizations must have a difference phase of $\pm 90^{\text{o}}$. In our RA design, it is selected a phase difference equals to $+90^{\text{o}}$ and in consequence, the circular polarization is LHCP. The opposite circular polarization, RCHP, can be produced if the linear polarization of the horn antenna is aligned to the x'-direction instead of the y'-direction (see axis in Fig. 9). The phase maps for both polarizations are displayed in Fig. 10. It is important to say that a constant phase reference can be added to the presented phase maps without introducing any error on the theoretical design of the reflectarray [5]. Nevertheless, this constant phase reference should be chosen carefully because it modifies the physical structure of the RA since the lengths of the tuning elements change accordingly. This implies that the unit cells located in the central zone of the RA, which has the greatest influence due to the amplitude taper, must respect a good linearity of the phase response with frequency. For the unit cell used, the performance of the RA is specially affected at the ends of the operating bandwidth. The phase maps presented in Fig. 10 produce satisfactory performances for the directivity and axial ratio (AR) in the considered frequency range.

Based on the computed phase maps, the physical implementation of these phase responses in the RA has been carried out by a lookup table that relates the lengths of the tuning element with their reflection phase values. This lookup table has been created with the simulated reflection phase shift values at 41 GHz and their corresponding tuning lengths. Due to the similarity of the phase response of the RA unit cell in normal

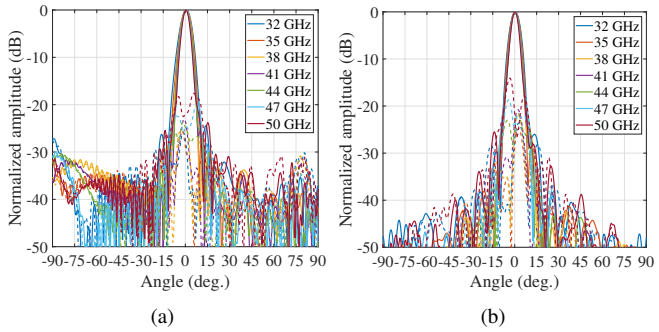

Fig. 11. Simulated results of the normalized radiation patterns of the reflectarray along the operating bandwidth: (a) for the E-plane and, (b) for the H-plane. The solid and dashed lines correspond to LHCP and RHCP, respectively.

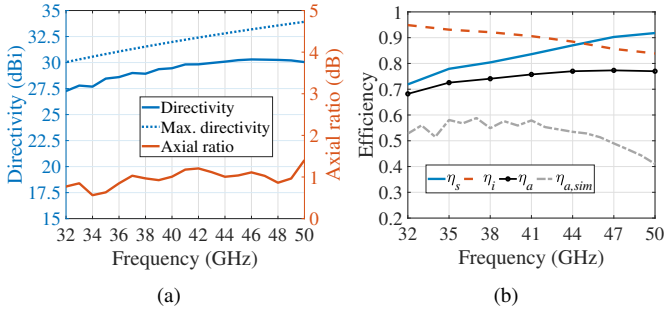

Fig. 12. (a) Simulated directivity, maximum achievable directivity and AR at the main beam direction. (b) Efficiency of the RA along the frequency.

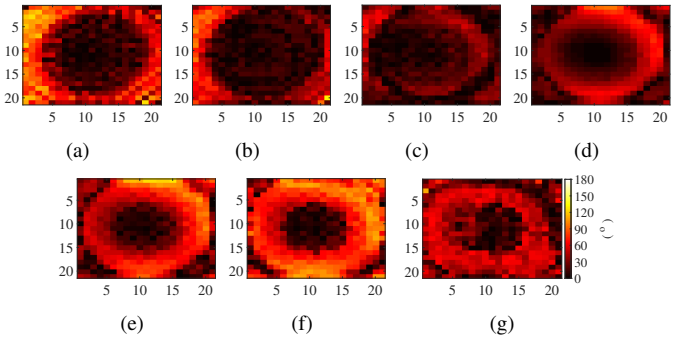

Fig. 13. Error phase maps for V-pol at different frequencies: (a) 32 GHz, (b) 35 GHz, (c) 38 GHz, (d) 41 GHz, (e) 44 GHz, (f) 47 GHz and, (g) 50 GHz.

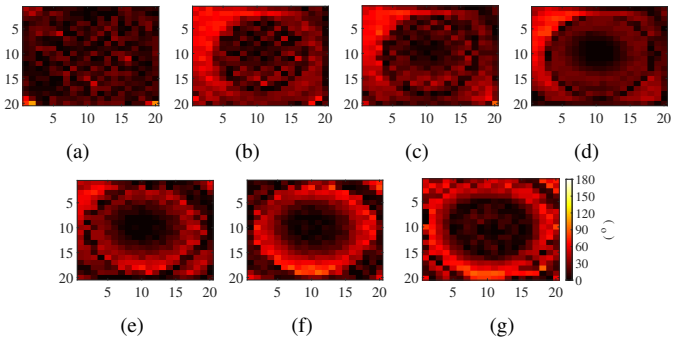

Fig. 14. Error phase maps for H-pol at different frequencies: (a) 32 GHz, (b) 35 GHz, (c) 38 GHz, (d) 41 GHz, (e) 44 GHz, (f) 47 GHz and, (g) 50 GHz.

and oblique incidence, each "phase - tuning length" entry of the lookup table is extracted from the simulated results of the unit cell at normal incidence. In this manner, the robustness of the unit cell phase response is examined in a RA where the unit cells receive different oblique incidence angles Fig. 11 presents the simulated results of the considered RA. The metal considered in the simulations is silver ($\sigma = 6.3 \cdot 10^7$ S/m). Normalized radiation patterns for LHCP and RHCP in their principal cuts, E-plane and H-plane, are shown in Fig. 11(a) and 11(b), respectively. The E-plane corresponds to the Z'Y' plane (see Fig. 9(a)) while, the H-plane is referred to the plane Z'X' when the z' axis is aligned with the main beam direction; this is $\phi = 90^o$ and $\theta = 20^o$. From the simulated normalized patterns displayed in Figs. 11(a) and 11(b), it can be observed the stability of the main beam direction for LHCP as well as a secondary lobe level below -20 dB along the entire frequency range. The cross polarization, which is RHCP, is around 20 dB lower than the LHCP in almost the entire considered band with the exception of the high end of frequencies.

In Fig. 12(a), the provided directivity and AR by the RA are presented. Additionally, the maximum directivity that the reflectarray can produce is also included. The achieved directivity ranges from 27.25 dBi to 30.3 dBi with an AR below 1.5 dB for the entire frequency range. To calculate the different efficiencies that impact the aperture efficiency of the RA, the analysis presented in [30] has been used. The coefficients q and q_e of the cosine models of the feed antenna and RA unit cell radiation patterns have been obtained by simulation. Since a large frequency range is considered, these coefficients vary with frequency and consequently, the amplitude taper in the plane of the reflectarray also changes with frequency. The range of values for q is from 9.5 to 20 while q_e goes from 0.5 to 0.85. The illumination efficiency (η_i) and spillover efficiency (η_s) over the frequency are presented in Fig. 12(b). In addition to these two efficiencies, the aperture efficiency (η_a) resulting from the product of η_i and η_s and, the aperture efficiency obtained in simulation ($\eta_{s,sim}$), which is calculated by the difference between the maximum achievable directivity and the produced directivity, are shown [see Fig. 12(a)]. We can observe that η_a is between 68% and 77% while $\eta_{a,sim}$ is not greater than 58%. This difference is due to additional efficiency factors considered in the full-wave simulation, which decrease η_a. Thanks to the metal-only structure of the RA, the material losses, in this case metal, are very low and a simulated radiation efficiency is above 97% in the frequency range.

Other efficiency factors such as blockage efficiency or return loss efficiency are negligible in our RA design. This is because the feed antenna illuminates the RA at oblique incidence and the reflection coefficient of the horn antenna is around -25 dB in the considered frequency range. Another relevant efficiency factor is the phase efficiency that takes into account the deviation from the desired phase distribution at RA aperture. Error phase maps have been calculated to observe the phase deviation produced at different frequencies. The calculation of these errors has been carried out by the difference between the desired phase distribution in the RA aperture and the one extracted, in the plane of the aperture,

TABLE I
SOURCE OF LOSSES (IN DECIBELS) IN THE REFLECTARRAY ANTENNA SYSTEM

RA unit cell	Feed antenna	Spillover	Illumination	Phase error
0.01 - 0.07	0.04 - 0.15	0.36 - 1.42	0.22 - 0.75	0.94 - 2.73

with CST Studio Suite. It is important to point out that for a correct calculation of the phase distribution in this aperture, the effect of the incident wave in simulation must be removed and only the wave reflected by the RA must be considered. The error phase maps for V-pol and H-pol at different frequencies are shown in Fig. 13 and Fig. 14, respectively. Phase errors located in the central area of RA are the ones that degrade performance the most, since this is the area that receives most of the illumination from the feed antenna. The cause of these phase errors is due to the perturbation of the unit cell phase response by the non-periodic environment, the modification of the oblique incidence angle across the RA and the non-perfect phase behavior of the unit cell in frequency. Nevertheless, in general, we do not find very large phase errors along the frequency for the two polarizations in the proposed RA design. In addition, it can be observed how the phase errors are greater at the higher frequencies of the operating band. This results in a reduction of the phase efficiency. Additionally, it is relevant to note that there is some loss in the polarization efficiency due to the excitation of the cross-polar component in certain areas of the RA. This produces an undesired radiation around the specular direction. These efficiency factors decrease the η_a. By taking into account the phase responses at different frequencies in the RA design process combined with an optimization algorithm, an improved aperture efficiency could be achieved. Nevertheless, this would lead to a higher computational cost in the design process. Table I summarizes the sources of losses that are present in the proposed RA design over the considered frequency band.

IV. FABRICATION, MEASUREMENTS AND DISCUSSION

In order to experimentally verify the design process presented in the previous sections, the RA has been fabricated and characterized in the anechoic chamber of University of Granada. A photo of the prototype is shown in Fig. 15(a). Thanks to the geometry of the proposed unit cell, it can be easily manufactured in 3D printing allowing a low cost and low weight prototype. Indeed, the manufacturing process followed for the prototype is based on stereolithography (SLA) 3D printing and a subsequent silver metallization. The printer used was the Form 3 from Formlabs with the high temp resin that allows a high precision printing with a thickness layer of 25 μm. The 3D printer achieves a XY resolution of 25 μm and the laser spot size is 85 μm. In relation to the tolerances, for feature size lower than 4 mm, the standard deviation is 30 μm. These properties in the 3D printing process produce a reliable manufacturing of the proposed reflectarray design. Regarding the metallization process, it was carried out by JetMetal [31], a company that offers a silver coating in plastic

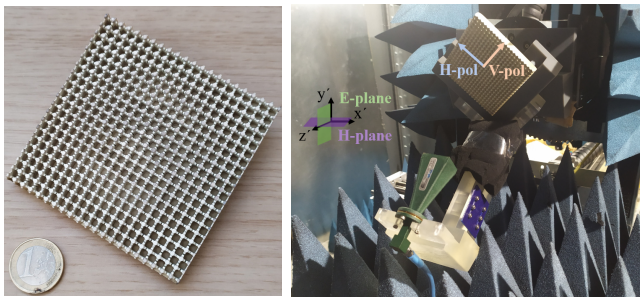

(a) (b)

Fig. 15. (a) Prototype of the RA design. (b) Setup to measure the RA.

pieces by means of spray metallization. The silver coating has a thickness of 2.5 μm which is approximately 7 times the skin depth for the minimum operating frequency. According to [32], the average roughness produced in this metallization process is 2 μm which reduces the conductivity achieved by the silver. This decrease in the conductivity is almost negligible since it maintains the conductivity around $3{\cdot}10^7$ S/m.

In Fig. 15(b), the implementation of the RA system is displayed. Some supports have been printed with the same 3-D printer to align the feeding horn with the center of the RA and the main beam direction of the RA with the receiving horn antenna of the measurement setup. The comparison between simulated and measured radiation patterns in the E- and H-planes for the LHCP and RHCP are presented in Fig. 16. We can observe a remarkable agreement for both the co- and cross-polarization at different frequencies. The half power beam width (HPBW) at 35 GHz, 41 GHz and 47 GHz are approximately 7º, 6º, 5º, respectively. In the HPBW, the maximum levels of cross-polar component, both simulated and measured, are -24.8 $\text{dB}^{sim.}_{35GHz}$, -27.5 $\text{dB}^{meas.}_{35GHz}$, -20.8 $\text{dB}^{sim.}_{41GHz}$, -24.1 $\text{dB}^{meas.}_{41GHz}$, -18.7 $\text{dB}^{sim.}_{47GHz}$ and -16.3 $\text{dB}^{meas.}_{47GHz}$. It can be noted that the cross-polar component increases with frequency. In order to complete the assessment of the proposed RA and to report more information about its radiation pattern performance, Figs. 17 and 18 show the measured 3-D LHCP and RHCP at different frequencies. In Fig. 17, we can observe the narrowing of the main beam as the frequency increases and, the appearance of side lobe levels at $\phi = 45º$ or 135º. Nevertheless, the maximum side lobe level is not greater than -20 dB. On the other hand, in Fig. 18, it is more clearly seen how the RHCP level increases with frequency and around the main beam zone. At 50 GHz, the highest level of cross-polar is achieved and it is -12.3 dB.

Fig. 19 illustrates the measured AR for different frequencies in the considered bandwidth. A 3-D acquisition has been carried out to observe how the AR behaves for different azimuth and elevation angles up to $\theta = 20º$. From this figure, we can observe the low value for AR around the main direction of the RA and how it is maintained along the frequency. It is noted a decrease in the angular region where the AR is below 3 dB as the frequency increases. The reason for this is because of the increase of the RHCP around the main direction with frequency. This leads to the cross-pol discrimination being below 15 dB and hence to the AR being greater than 3 dB [33].

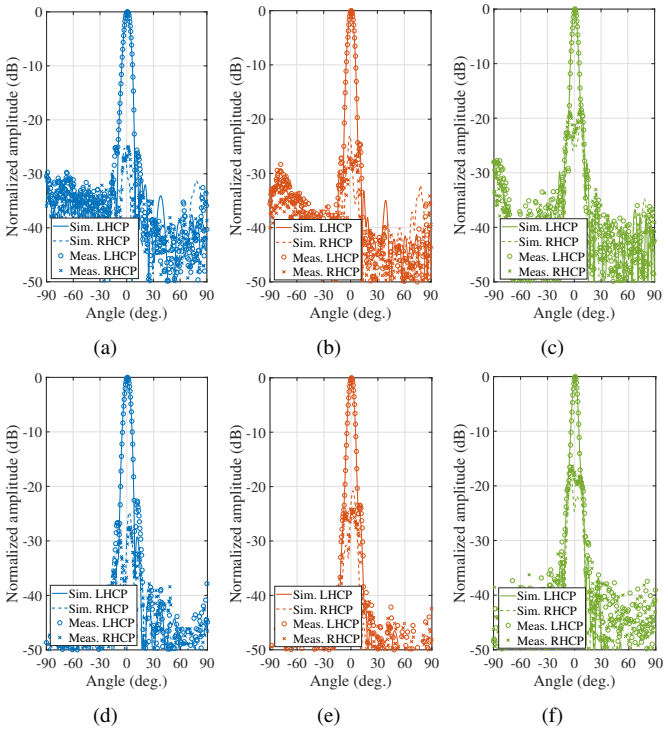

Fig. 16. Simulated and measured results of the normalized radiation patterns of the reflectarray along the operating bandwidth. For the E-plane: (a) at 35 GHz, (b) at 41 GHz and, (c) at 47 GHz. For the H-plane: (d) at 35 GHz, (e) at 41 GHz and, (f) at 47 GHz.

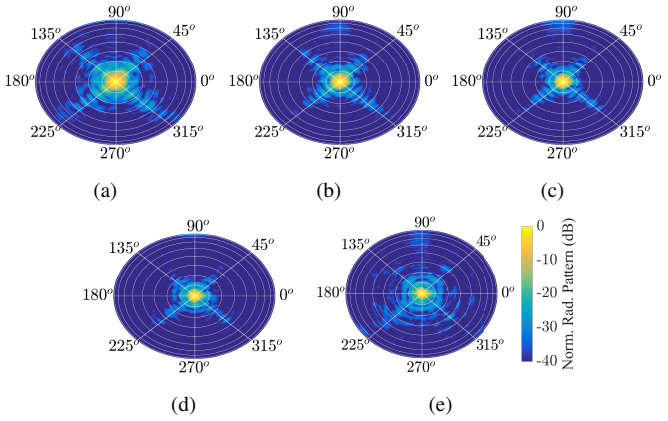

Fig. 17. Measured 3-D LHCP at different frequencies: (a) 32 GHz, (b) 36.5 GHz, (c) 41 GHz, (d) 45.5 GHz and, (e) 50 GHz. The radial lines mark the azimuth angles ϕ while their intersection with the concentric circles mark the elevation angles θ. The angular distance between each concentric circle is 10º.

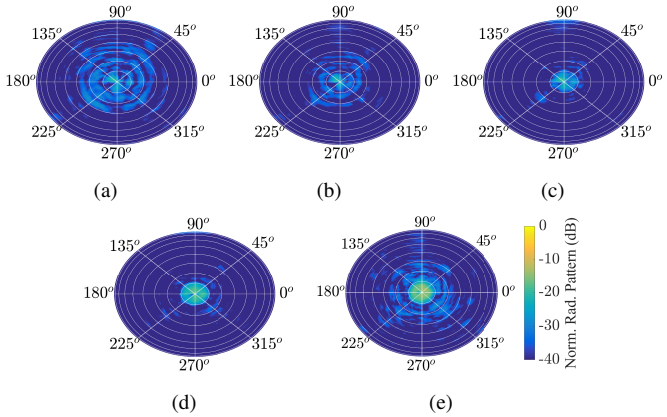

Fig. 18. Measured 3-D RHCP at different frequencies: (a) 32 GHz, (b) 36.5 GHz, (c) 41 GHz, (d) 45.5 GHz and, (e) 50 GHz. The angle of the radial lines mark the azimuth angles ϕ while their intersection with the concentric circles mark the elevation angles θ. The angular distance between each concentric circle is 10º.

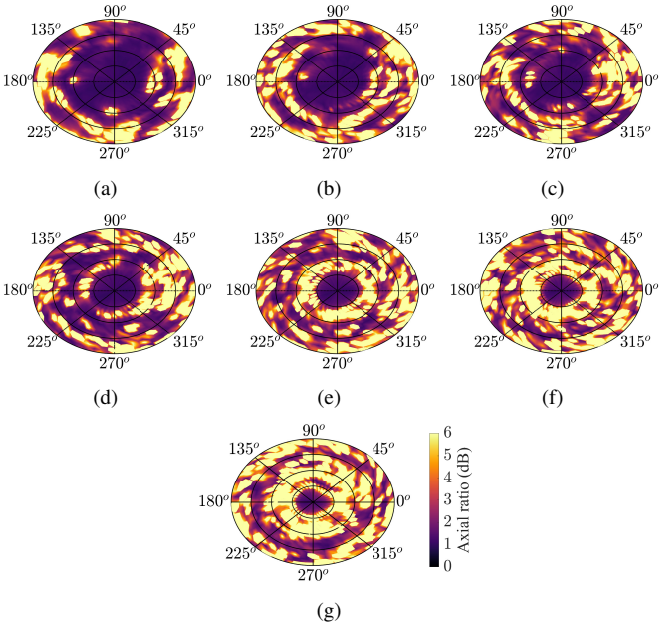

Fig. 19. Measured 3-D axial ratio at different frequencies: (a) 32 GHz, (b) 35 GHz, (c) 38 GHz, (d) 41 GHz, (e) 44 GHz, (f) 47 GHz and, (g) 50 GHz. The angle of the radial lines mark the azimuth angles ϕ while their intersection with the concentric circles mark the elevation angles θ. The angular distance between each concentric circle is 5º.

To conclude with the RA characterization, Fig. 20 presents a comparison of the simulated and measured results for the realized gain and AR in the main beam direction. Both the realized gain and the measured AR are very close to the results obtained in simulation. This good agreement in the measured realized gain indicates that the high radiation efficiency is also obtained in the fabricated RA. Besides, the measured 3-dB AR bandwidth is also covered over the considered frequency range.

A performance comparison with the state-of-the-art metal-only RAs is done. Table II presents the main features of comparison between the proposed RA design and those reported in the literature. In this work, a wider 3-dB gain bandwidth with similar peak aperture efficiency is obtained compared to the other works. However, we can highlight that it is the first metallic RA that allows the control of both incident linear polarizations in addition to produce a large 3-dB AR bandwidth (43.9%). Recent work in [34] also achieves the independent control but for orthogonal circular polarizations. Its operating bandwidth is below millimeter frequencies with a lower peak aperture efficiency and 3-dB gain bandwidth regarding the proposed RA.

For the sake of completeness, Table III shows a comparison with the state-of-the-art works about fully-dielectric RAs in millimeter-wave frequencies. To make a fair comparison, the

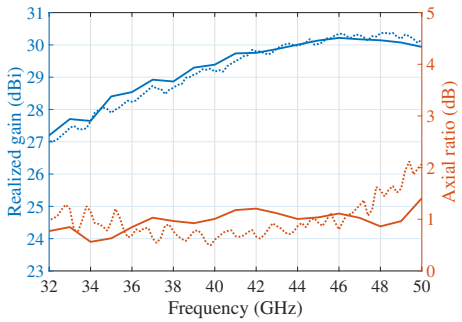

Fig. 20. Simulated and measured realized gain and AR at the main beam direction. The solid and dashed lines correspond to simulated and measured results, respectively.

included works either produce circular polarization or independently control the incident linear polarizations. It can be seen that although the other works can achieve similar 3-dB gain and AR bandwidths, the aperture efficiency is lower than the one obtained with the proposed RA. This is because it is difficult to find dielectrics with lower losses than metal in this frequency range and thus, metal-only RAs achieve higher radiation efficiency. Particular attention should be paid to the work in [35]. In that work, a unit cell design that controls the phase of both orthogonal incident polarizations by modifying the length of dielectric cuboids has been proposed. Nevertheless, the unit cell design relies on dielectrics, unlike the RA unit cell proposed in this work, which only uses metal in its structure. One of the consequences of using only metallic structures is the strong boundary conditions they impose, which in our design allow a negligible phase variation of the orthogonal polarization (lower than 1°). In contrast, the dielectric RA unit cell presented in [35] shows high phase variation for the polarization that is not intended to be modified. Additionally, our RA design mitigates the shadowing effect that appears in [35] and [36] since all the RA unit cells have the same length (L in Fig. 1). A high aperture efficiency is also obtained in this work with wider 3-dB gain bandwidth. Finally, it is noteworthy to say that thanks to the performance offered by the proposed RA unit cell, the 3-dB AR bandwidth is extended but in the presented results we have only considered the standard frequency band supported by WR22 waveguide.

V. Conclusions

A metal-only RA design that allows the phase control of impinging orthogonal polarizations is presented in this paper. Based on a unit cell with 3-D geometry, an independent phase tuning in a wide frequency range is achieved. In each unit cell, the modification of the reflected phase is implemented by the variation of the lengths of some metallic blocks in the propagating path of the wave inside the RA unit cell. The simulated results reveal a fairly linear reflected phase response along the frequency with high level of independent phase tuning in both orthogonal polarizations. In addition, this performance is maintained up to an angle of approximately 30° in oblique incidence. Thanks to this performance provided by the RA unit cell, a circularly-polarized RA antenna is designed. The RA is rotated by 45° regarding the linearly-polarized feed antenna to excite both polarizations in the unit cells that compose the RA. A prototype is fabricated and the measured results agree with the ones obtained in simulation. The presented RA antenna, which operates from 32 GHz to 50 GHz, produces a 3-dB gain bandwidth of 40.96% with a 2-dB AR bandwidth of 43.9%. Besides, the measured AR performs well in azimuth and elevation angles keeping the minimum values for AR around main beam direction. Finally, the measured realized gain has good agreement with the simulated one providing a radiation efficiency greater than 97% with a peak aperture efficiency of 55.4%.

TABLE II
Comparison between the proposed RA and reported metal-only RAs

Ref.	Center freq. (GHz)	3-dB Gain bandwidth	Peak aperture efficiency	Dual-pol control	3-dB AR bandwidth
[8]	60	10%	35%	No	26.5%
[10]	60	16.67%	60.3%	No	n. a.
[12]	75	9.2%	30.2%	No	n. a.
[15]	100	22.2%	50.1%	No	n. a.
[16]	94	19.8%	44.8%	No	n. a.
[17]	12.3	9.75%*	50%	No	n. a.
[18]	38	10.5%	n. a.	No	n. a.
[20]	9.3	24.2%*	50.6%	No	25%
[21]	27	22.2%	n. a.	No	n. a.
[34]†	27	18.2%	38%	Yes	18.2%
This work	41	40.96%	55.4%	Yes	43.9%

* 1-dB gain bandwidth.
† Independent control of circular polarizations.

TABLE III
Comparison between the proposed RAs and reported fully-dielectric RA at millimeter-waves

Ref.	Center freq. (GHz)	3-dB Gain bandwidth	Peak aperture efficiency	Radiation efficiency*	3-dB AR bandwidth
[35]	33	30%	34%	88.5%	42.7%
[37]	31	37.5%	32.5%	63% - 89%	43.2%
[38]	35	28.57%	16.4%	88.5%	n. a.
[39]	30	17.24%	16.5%	20% - 50%	19.3%
This work	41	40.96%	55.4%	97% - 99%	43.9%

* If the value is not given explicitly, it is calculated from the reflection losses of the RA unit cell.

Acknowledgment

The authors would like to thank Carmelo García-García for his help in the measurements and the spanish company Carlos Valero S.L. for its help and expertise in the metallization process.

References

[1] C. K. Anjinappa, F. Erden and I. Güvenç, "Base station and passive reflectors placement for urban mmWave networks," *IEEE Trans. Veh. Technol.*, vol. 70, no. 4, pp. 3525-3539, April 2021.

[2] W. Khawaja, O. Ozdemir, Y. Yapici, F. Erden and I. Guvenc, "Coverage enhancement for NLOS mmWave links using passive reflectors," *IEEE Open Journal of the Communications Society*, vol. 1, pp. 263-281, 2020.

[3] M. Di Renzo *et al.*, "Smart radio environments empowered by reconfigurable intelligent surfaces: how it works, state of research, and the road ahead," *IEEE J. Sel. Areas Commun.*, vol. 38, no. 11, pp. 2450-2525, Nov. 2020.

[4] C. Molero *et al.*, "Metamaterial-based reconfigurable intelligent surface: 3D meta-atoms controlled by graphene structures," *IEEE Commun. Mag.*, vol. 59, no. 6, pp. 42-48, June 2021.

[5] P. Nayeri, F. Yang, and A. Z. Elsherbeni, *Reflectarray antennas: theory, designs, and applications*. USA: Wiley, 2018.

[6] H. Chou, Y. Chen and H. Ho, "An all-metallic reflectarray and its element design: exploring the radiation characteristics of antennas for directional beam applications," *IEEE Antennas Propag. Mag.*, vol. 60, no. 5, pp. 41-51, Oct. 2018.

[7] R. Deng, F. Yang, S. Xu and M. Li, "A low-cost metal-only reflectarray using modified slot-type phoenix element with 360° phase coverage," *IEEE Trans. Antennas Propag.*, vol. 64, no. 4, pp. 1556-1560, April 2016.

[8] K. Q. Henderson and N. Ghalichechian, "Circular-polarized metal-only reflectarray with multi-slot elements," *IEEE Trans. Antennas Propag.*, vol. 68, no. 9, pp. 6695-6703, Sept. 2020.

[9] Y. G. Antonov, M. I. Sugak, S. V. Ballandovich, G. A. Kostikov and L. M. Liubina, "Design of wideband reflectarray antennas," in *2020 14th European Conference on Antennas and Propagation (EuCAP)*, 2020, pp. 1-5.

[10] Y. H. Cho, W. J. Byun and M. S. Song, "Metallic-rectangular-grooves based 2D reflectarray antenna excited by an open-ended parallel-plate waveguide," *IEEE Trans. Antennas Propag.*, vol. 58, no. 5, pp. 1788-1792, May 2010.

[11] D. Wang, R. Gillard, and R. Loison, "A 60 GHz passive repeater array with quasi-endfire radiation based on metal groove unit-cells," *Int. J. Microw. Wirel. Technol.*, vol. 8, no. 3, pp. 431–436, 2016.

[12] Y. H. Cho, W. J. Byun and M. S. Song, "High gain metal-only reflectarray antenna composed of multiple rectangular grooves," *IEEE Trans. Antennas Propag.*, vol. 59, no. 12, pp. 4559-4568, Dec. 2011.

[13] G. -B. Wu, Y. -S. Zeng, K. F. Chan, B. -J. Chen, S. -W. Qu and C. H. Chan, "High-gain filtering reflectarray antenna for millimeter-wave applications," *IEEE Trans. Antennas Propag.*, vol. 68, no. 2, pp. 805-812, Feb. 2020.

[14] B. Chen, H. Yi, K. B. Ng, S. Qu and C. H. Chan, "3D printed reflectarray antenna at 60 GHz," in *2016 International Symposium on Antennas and Propagation (ISAP)*, 2016, pp. 92-93.

[15] R. Deng, F. Yang, S. Xu and M. Li, "A 100-GHz metal-only reflectarray for high-gain antenna applications," *IEEE Antennas Wirel. Propag. Lett.*, vol. 15, pp. 178-181, 2016.

[16] W. Lee and Y. J. Yoon, "A broadband dual-metallic-reflectarray antenna for millimeter-wave applications," *IEEE Antennas Wirel. Propag. Lett.*, vol. 16, pp. 856-859, 2017.

[17] H. Chou, C. Lin and M. Wu, "A high efficient reflectarray antenna consisted of periodic all-metallic elements for the Ku-band DTV applications," *IEEE Antennas Wirel. Propag. Lett.*, vol. 14, pp. 1542-1545, 2015.

[18] H. Chou and J. W. Liu, "Synthesis and characteristic evaluation of convex metallic reflectarray antennas to radiate relatively orthogonal multi-beams," *IEEE Trans. Antennas Propag.*, vol. 66, no. 8, pp. 4008-4016, Aug. 2018.

[19] B. Zhang, C. Jin, Q. Lv, J. Chen and Y. Tang, "Low-RCS and wideband reflectarray antenna with high radiation efficiency," *IEEE Trans. Antennas Propag.*, vol. 69, no. 7, pp. 4212-4216, July 2021.

[20] G. Kong, X. Li, Q. Wang and J. Zhang, "A wideband reconfigurable dual-branch helical reflectarray antenna for high-power microwave applications," *IEEE Trans. Antennas Propag.*, vol. 69, no. 2, pp. 825-833, Feb. 2021.

[21] P. Mei, S. Zhang and G. F. Pedersen, "A low-cost, high-efficiency and full-metal reflectarray antenna with mechanically 2-D beam-steerable capabilities for 5G applications," *IEEE Trans. Antennas Propag.*, vol. 68, no. 10, pp. 6997-7006, Oct. 2020.

[22] S. M. A. Momeni Hasan Abadi and N. Behdad, "Broadband true-time-delay circularly polarized reflectarray with linearly polarized feed," *IEEE Trans. Antennas Propag.*, vol. 64, no. 11, pp. 4891-4896, Nov. 2016.

[23] C. Molero Jimenez, E. Menargues and M. García-Vigueras, "All-metal 3-D frequency-selective surface with versatile dual-band polarization conversion," *IEEE Trans. Antennas Propag.*, vol. 68, no. 7, pp. 5431-5441, July 2020.

[24] J. Velasco, I. Parellada-Serrano, and C. Molero, "Fully metallic reflectarray for the Ku-band based on a 3D architecture," *Electronics*, vol. 10, no. 21, p. 2648, Oct. 2021.

[25] C. Molero, H. Legay, T. Pierré and, M. García-Vigueras, "Broadband 3D-printed polarizer based on metallic transverse electro-magnetic unit-cells" *IEEE Trans. Antennas Propag.*, vol. 70, no. 6, pp. 4632-4644, June 2022.

[26] Y. He, Z. Gao, D. Jia, W. Zhang, B. Du and Z. N. Chen, "Dielectric metamaterial-based impedance-matched elements for broadband reflectarray," *IEEE Trans. Antennas Propag.*, vol. 65, no. 12, pp. 7019-7028, Dec. 2017.

[27] Á. Palomares-Caballero, C. Molero, P. Padilla, María García-Vigueras, and Raphaël Gillard, "Metal-only reflectarray unit cell for dual-polarization control," in *2022 16th European Conference on Antennas and Propagation (EuCAP)*, 2022.

[28] S. D. Targonski and D. M. Pozar, "Minimization of beam squint inmicrostrip reflectarrays using an offset feed," in *Proc. IEEE Antennas Propag. Soc. Int. Symp.*, Baltimore, MD, USA, Jul. 1996.

[29] E. Plaza, G. Leon, S. Loredo and F. Las-Heras, "A simple model for analyzing transmitarray Lenses," *IEEE Antennas Propag. Mag.*, vol. 57, no. 2, pp. 131-144, April 2015.

[30] A. Yu, F. Yang, A. Z. Elsherbeni, J. Huang, and Y. R. Samii, "Aperture efficiency analysis of reflectarray antennas," *Microw. Opt. Technol. Lett.*, vol. 52, no. 2, pp. 364–372, Feb. 2010.

[31] Jet Metal Tecnnologies. *Metallization principle*. Accessed: Jun. 2022. [Online]. Available: http://jetmetal-tech.com

[32] W. Feuray *et al.*, "Evaluation of metal coating techniques up to 66 GHz and their application to additively manufactured bandpass filters," in *2017 47th European Microwave Conference (EuMC)*, 2017, pp. 512-515.

[33] C. Pfeiffer and B. Tomasic, "Multi-octave linear-to-circular polarizers," in *2017 IEEE International Symposium on Antennas and Propagation & USNC/URSI National Radio Science Meeting*, 2017, pp. 673-674

[34] J. Zhu, S. Liao, S. Li and Q. Xue, "Additively manufactured metal-only millimeter-wave dual circularly polarized reflectarray antenna with independent control of polarizations," *IEEE Trans. Antennas Propag.*, 2022, doi: 10.1109/TAP.2022.3184474.

[35] Q. Cheng *et al.*, "Dual circularly polarized 3D printed broadband dielectric reflectarray with a linearly polarized feed," *IEEE Trans. Antennas Propag.*, vol. 70, no. 7, pp. 5393-5403, July 2022.

[36] P. Nayeri, M. Liang, R. A. Sabory-García, M. Tuo, F. Yang, M. Gehm, H. Xin, and A. Z. Elsherbeni, "3D printed dielectric reflectarrays: low-cost high-gain antennas at sub-millimeter waves," *IEEE Trans. Antennas Propag.*, vol. 62, no. 4, pp. 2000–2008, 2014.

[37] P. Mei, S. Zhang and G. F. Pedersen, "A wideband 3-D printed reflectarray antenna with mechanically reconfigurable polarization," *IEEE Antennas Wirel. Propag. Lett.*, vol. 19, no. 10, pp. 1798-1802, Oct. 2020.

[38] Y. -X. Sun, D. Wu and J. Ren, "Millimeter-wave dual-polarized dielectric resonator reflectarray fabricated by 3D printing with high relative permittivity material," *IEEE Access*, vol. 9, pp. 103795-103803, 2021.

[39] B. Li, C. Y. Mei, Y. Zhou and X. Lv, "A 3-D-printed wideband circularly polarized dielectric reflectarray of cross-shaped element," *IEEE Antennas Wirel. Propag. Lett.*, vol. 19, no. 10, pp. 1734-1738, Oct. 2020.